Large-Surface-Area $Bi_2Sn_2O_7$ Quantum Dots for Room-Temperature 1-Octanol Sensing: A Combined Experimental and DFT Study

Yiwen Zhou[a,b], Zichen Zheng[a,b,c], Kewei Liu[a,b,d], Marc Debliquy[d], Carla Bittencourt[c], Chao Zhang[a,b,*]

a. College of Mechanical Engineering, Yangzhou University, Yangzhou 225127, PR China
b. Jiangsu Key Laboratory of Surface Strengthening and Functional Manufacturing, Yangzhou University, Yangzhou 225127, PR China
c. Chimie des Interactions Plasma-Surface, Research Institute for Materials Science and Engineering, University of Mons, 7000 Mons, Belgium
d. Service de Science des Matériaux, Research Institute for Materials Science and Engineering, Faculté Polytechnique, University of Mons, 7000 Mons, Belgium

* Corresponding author
Prof. Chao Zhang
College of Mechanical Engineering
Yangzhou University
Huayang West Road 196
Yangzhou 225127, Jiangsu Province
P.R. China
Tel/Fax: +86-514-87971980
Email: zhangc@yzu.edu.cn

Abstract

Chemiresistive gas sensors (CGSs) designed for the detection of agricultural volatile organic compounds (VOCs) play a crucial role in monitoring crop growth and ensuring the quality of agricultural products. However, conventional metal oxide gas sensors continue to encounter challenges related to high power consumption and limited detection capabilities. In this study, bismuth stannate oxide $Bi_2Sn_2O_7$ (BSO) quantum dots (QDs) were synthesized via a hydrothermal method to facilitate room-temperature (RT) detection of 1-octanol. A systematic investigation was conducted to elucidate the relationship between the gas-sensing performance of the material and its microstructure, surface valence states, and electronic structure. The BSO-8 sensor, characterized by an exceptionally high specific surface area (BET=143.57 m^2g^{-1}), demonstrated a wide detection range of 1 to 50 ppm, exhibiting a remarkable response of 75.06±1.25 at 50 ppm under 30% relative humidity. Additionally, the sensor displayed excellent reproducibility, long-term stability, and significant selectivity toward 1-octanol. Further mechanistic insights were obtained through valence band spectroscopy (VB-XPS) and density functional theory (DFT) calculations, which provided a comprehensive understanding of the evolution of the electronic structure and gas adsorption behavior. These findings demonstrate the potential of BSO-based sensors for practical applications in detecting 1-octanol at 30%RH, highlighting its significance as a key biomarker for agricultural VOCs.

Key Words: Gas sensor, Room temperature, $Bi_2Sn_2O_7$, alkali etching, DFT calculation

1-Octanol, a volatile organic compound (VOC), is widely used in chemical manufacturing, pharmaceuticals, and food processing. Recently, it has been identified as an agricultural VOC emitted under stress conditions in crops, serving as a crucial indicator for predicting infections and inhibiting mold growth [1,2]. Additionally, this gas compound can act as a marker for grain aging and assess flavor quality [3,4]. In the quality monitoring of agricultural products, most detection methods still rely on techniques such as gas chromatography-mass spectrometry (GC-MS), which require expensive, large-scale equipment, specialized technical skills, and lengthy procedures, complicating simple, real-time monitoring [5]. Such limitations significantly hinder the practical application of these detection systems. Therefore, the development of efficient and cost-effective gas sensors has become essential. Among the alternatives, portable sensing devices have emerged as effective solutions and have gained considerable attention. In particular, CGSs gas sensors operate by detecting the electron transfer generated from chemical reactions between target gas molecules and the sensing layer on interdigitated electrodes (IDEs), converting these interactions into measurable electrical signals [6,7]. Due to their inherent sensing principles, this mechanism enables selective detection of specific target gases. Therefore, modifying sensing materials remains a crucial direction for enhancing sensor performance.

Recent advancements in nanomaterials, particularly metal oxides, have opened new avenues for improving gas sensors performance. Metal oxides are

known for their semiconducting properties, high stability, and ability to undergo surface reactions with target gases [8,9]. However, achieving room temperature operation and a wide detection range are still critical challenges for gas sensors, as these features eliminate the need for complex heating elements, making the sensors more energy-efficient and suitable for portable applications[10,11].

$Bi_2Sn_2O_7$ (BSO), a representative pyrochlore-type oxide, possesses a distinctive electronic configuration characterized by spatially ordered $[SnO_6]^{6-}$ regular octahedra at vertex positions and corner-sharing $[Bi_4O]^{6+}$ tetrahedra (Figure 1a)[12]. This structural architecture facilitates electron transfer during surface-mediated gas adsorption and chemical reactions. Furthermore, as a ternary metal oxide, BSO exhibits advantageous physicochemical properties, including low work function, highly hybridized electronic orbitals, and easily generated oxygen vacancies that actively participate in band structure modulation, optimizing electron transport efficiency. Numerous reports have documented the application of BSO in photocatalytic nitrogen fixation[13,14]. Recent first-principles calculations have demonstrated that BSO[15], as an n-type oxide, exhibits superior electron/thermal transport characteristics at room temperature (RT), positioning it as a promising candidate for electrochemical gas sensing applications. The nanoscale design of the material further enhances the performance of gas sensors. Specifically, nanomaterials with a high specific surface area maximize gas-material interfacial contact, increase the exposure of surface defects, and optimize charge transfer kinetics during

gas adsorption and desorption cycles, significantly improving gas adsorption efficiency and promoting surface electron transfer processes. Consequently, BSO exhibits exceptional potential for RT gas detection technologies. However, its application in RT gas sensing has rarely been reported in the existing literature.

This study reports the novel application of $Bi_2Sn_2O_7$ (BSO) in room-temperature gas detection. Nanometer-scale BSO QDs, characterized by a large specific surface area and a high density of oxygen vacancies, were synthesized using a hydrothermal method with polyvinylpyrrolidone (PVP) as a reducing agent, followed by alkaline etching. The investigation systematically examined the microstructure and electronic properties of BSO, as well as its sensing performance toward 1-octanol. Additionally, first-principles calculations were employed to model the electronic transfer and analyze gas adsorption processes across various surface configurations. These findings contribute significantly to the development of ternary metal oxide gas sensors capable of effective operation at RT.

Experimental section

Synthesis of BSO. All chemicals were purchased from Shanghai Aladdin Biochemical Technology Co., Ltd. (AR grade) and used without further purification. BSO was synthesized via a facile hydrothermal method (Figure 1a). Specifically, 546 mg of mannitol was added to 30 mL of deionized (DI) water and stirred continuously until fully dissolved. Subsequently, 486 mg of Bi

$(NO_3)_3 \cdot 5H_2O$ and 0.4 g of polyvinylpyrrolidone (PVP) were added as a surfactant and reducing agent to the above solution to form Solution A. Then, 10 mL of $Na_2SnO_3 \cdot 3H_2O$ aqueous solution (containing 266 mg) was dripped into Solution A. Under stirring, x mL of Sodium hydroxide (NaOH) solution (2 wt.%) was added dropwise to the mixture, followed by additional stirring for 25 min. The synthesized precursor was placed in a 100 mL Teflon-coated stainless-steel autoclave and heated at 160°C for 24 hours, undergoing a self-assembly process to yield the precursor. The product was thoroughly rinsed with DI water and absolute ethanol. The obtained powder samples were designated as BSO-x, where x represents the volume of NaOH solution added (in milliliters), with values of x being 4, 6, 8, 10, and 12.

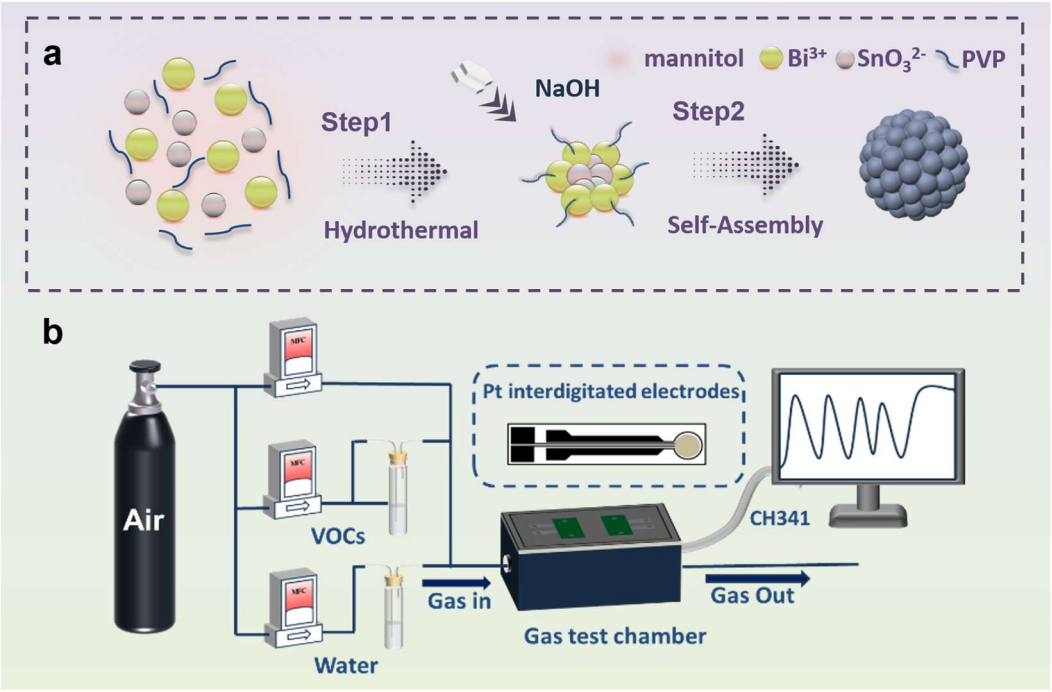

Figure 1. (a) Synthesis of BSO, (b) Homemade gas sensing system.

Experimental characterisation of the sensing material. The crystalline structures and phases of the synthesized samples were analyzed using X-ray diffraction (XRD) on a Bruker D8 Advance instrument. The microstructure and morphology were examined using a field emission scanning electron microscope (FE-SEM, S-4800, Japan), high-resolution transmission electron microscopy (HRTEM, Tecnai, Netherlands), and a high-angle annular dark-field scanning transmission electron microscope (HAADF-STEM) with energy-dispersive spectroscopy (EDS) was carried out to assess the element distribution. Optical band gaps were evaluated from UV-Vis-NIR absorption data (Cary 5000 system) using standard Tauc transformation methods The chemical states were assessed using X-ray photoelectron spectroscopy (XPS, Thermo Fisher ESCALAB250Xi, USA). An Autosorb IQ3 instrument (Quantachrome Instruments, USA) was employed to measure the Brunauer-Emmett Teller (BET) surface area and pore size distribution.

Gas sensor fabrication and measurements. The obtained powder was formulated into a suspension for drop-coating onto the sensor. Specifically, ~2 mg of BSO was homogenized with ~1 mL of deionized water through mechanical grinding to form a uniform suspension. This dispersion subsequently dropped onto the electrode region and dried for subsequent use. Prior to the gas sensing test, the film-coated sensor chip underwent a preconditioning protocol at 120°C for 12 h under an ambient atmosphere to ensure baseline signal stabilization.

Gas sensing performance tests were conducted using a homemade system (Figure 1b). Pt interdigitated electrodes were employed as planar test chips for gas-sensing measurements. The device architecture comprised an alumina substrate (6 × 30 mm) integrated with screen-printed platinum electrodes (thickness: 5 μm; inter-electrode gap: 0.42 mm). Gas-sensing performance was evaluated using a four-channel gas sensing analysis system (Wuhan Hua Chuang Rui Ke Technology Co., Ltd., Wuhan), consisting of Pt interdigitated electrodes; an aluminum alloy gas test chamber (equipped with CH341 serial port communication for data acquisition), and a dynamic gas-mixing apparatus (Figure 1b). The gas-mixing system employed three mass flow controllers (MFC, Bronkhorst, Netherlands) for precise gas blending. High-purity synthetic air (79% N_2+21% O_2) was supplied by Nanjing Special Gases Co., Ltd. Target gas concentrations were calibrated using saturated vapor equilibrium methodology (Equation 1)[16]. Gas concentration and relative humidity (RH) control adjustment according to Equations 2 and 3:

$$Intial\ concentration\ of\ VOCs\left(ppm\right)=\left(Vapor\ pressure\ of\ VOCs\ (mmgH)/760\times 10^{6}\right) \quad (1)$$

$$Adjustment\ concentration\ of\ VOCs\left(ppm\right)=\frac{Flow\ rate\ of\ VOCs}{Total\ flow} \quad (2)$$

$$Adjustment\ of\ RH\left(ppm\right)=\frac{Flow\ rate\ of\ Water}{Total\ flow} \quad (3)$$

For the n-type BSO sensor, the gas response was calculated using the ratio Ra/Rg, where Ra denotes the resistance in air, while Rg refers to the stabilized resistance in the presence of the target gas. The response time (τ_{res})

and recovery time (τ_{rec}) were determined as the duration required for the resistance variation to reach 90% of its maximum amplitude. All gas sensing measurements were conducted at room temperature (~25 °C), 30% RH.

Theoretical modelling to analyze gas adsorption processes. All first-principles calculations were conducted utilizing the CASTEP code implemented in Materials Studio 2020, with the generalized gradient approximation (GGA) in the Perdew-Burke-Ernzerhof (PBE) parametrization for exchange-correlation effects[17]. A plane-wave basis set with a 450 eV kinetic energy cutoff was implemented to ensure computational accuracy. The convergence criteria were set as 1×10^{-5} eV for total energy, 0.03 eV·Å^{-1} for maximum residual force, and 1×10^{-5} eV for energy difference between successive iterations. During structural optimization, a 5×5×5 Monkhorst-Pack grid was used for Brillouin zone sampling, whereas surface calculations were performed with a 2×2×1 k-point mesh corresponding to the (2 2 2) surface which exhibits a large number of dangling bonds and defects due to its relatively high surface energy. Interperiodic interference was minimized through the introduction of a 15 Å vacuum buffer along the z-coordinate. The optimization model is presented in Figure S1.

The adsorption energy (E_{ads}) of the target gas molecules on the surface can be quantified through Equation 4 [18]:

$$E_{ads} = E_{total} - (E_{surface} + E_{Vocs}) \quad (4)$$

where E_{total} denotes the total energy of surface ((222) of BSO)-target gas

adsorption system under equilibrium configuration, with $E_{surface}$ and E_{VOCs} representing the energy of the pristine cleaved surface and free gas molecule prior to adsorption, respectively.

Results and Dscussions

Morphology and Composition Analysis. TEM characterization of BSO (Figure S3) indicates an average particle size of less than 10 nm, with minimal variation observed. This small particle size enhances the exposure of surface atoms, thereby facilitating defect formation. The fine-tuning of particle size at the nanoscale is anticipated to positively affect the material properties through defect engineering, modsAR WQE321`ulation of the electronic structure, and an increase in specific surface area, as discussed in subsequent sections. Additionally, the ultrasmall crystallite dimensions may lead to quantum confinement effects that enhance charge carrier mobility, thereby improving gas-sensing performance. However, an excess of hydroxide ions (OH^-) may promote the dissolution and redeposition of small quantum dots, contributing to the growth of larger particles, exacerbating agglomeration, and increasing particle size. These changes could diminish size-dependent effects and negatively impact gas sensing performance. **Figures 2a** and **2b** display TEM images of BSO-8, illustrating its nanoscale morphology, while the SEM images of BSO-8 are presented in Figure S4. The BSO-8 particles are approximately 5-6 nm in size and consist of bismuth, tin, and oxygen atoms (Figure. 2c). To further investigate, we conducted HRTEM studies. HRTEM analysis (Figure 2d)

is in close agreement with the JCPDS reference card (No. 87-0284), indicating a lattice spacing of d=0.317 nm corresponding to the (222) crystallographic plane, with parameters *a*=*b*=*c*=10.72A˚ and *α*=*β*=*γ*=90°, as derived from Fourier Transform (FFT) (Figures 2e and 2f). This suggests growth along the [001] direction [12,19]. The network structure offers advantages for carrier transport. The SAED pattern (Figure 2e (insert)) further confirms the crystallographic alignment with the (422) and (222) planes, while EDX spectra (Figure S5) and EDS elemental mapping (Figure 2h) verifies the existence and uniform spatial distribution of Bi, Sn, and O components.

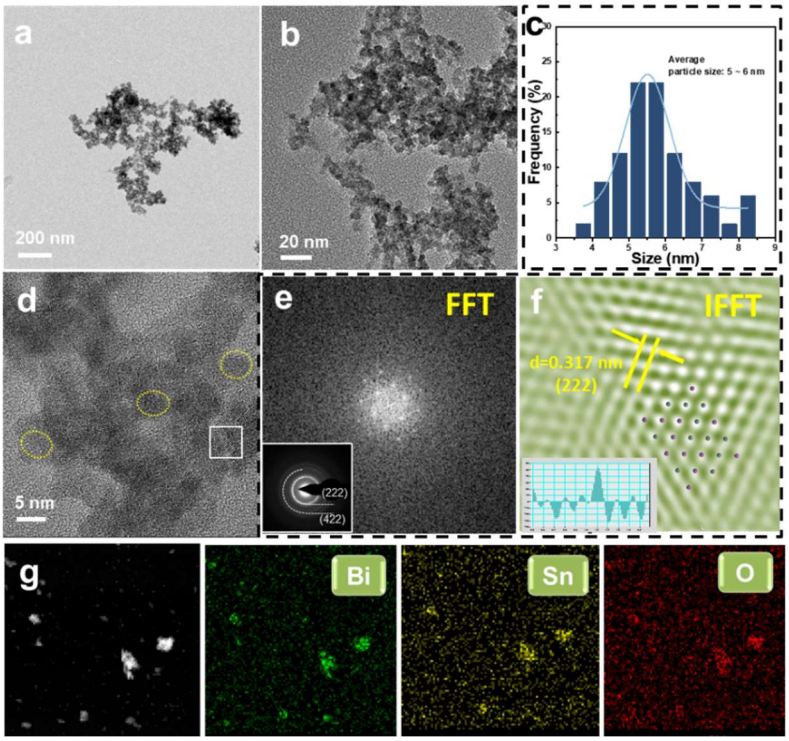

Figure 2. (a)(b) TEM image, (c) particle size distribution, (d) HRTEM, (e) the corresponding FFT pattern (The insets show the SAED pattern) and (f) IFFT pattern, (g) HAADF-STEM elemental mapping of BSO-8.

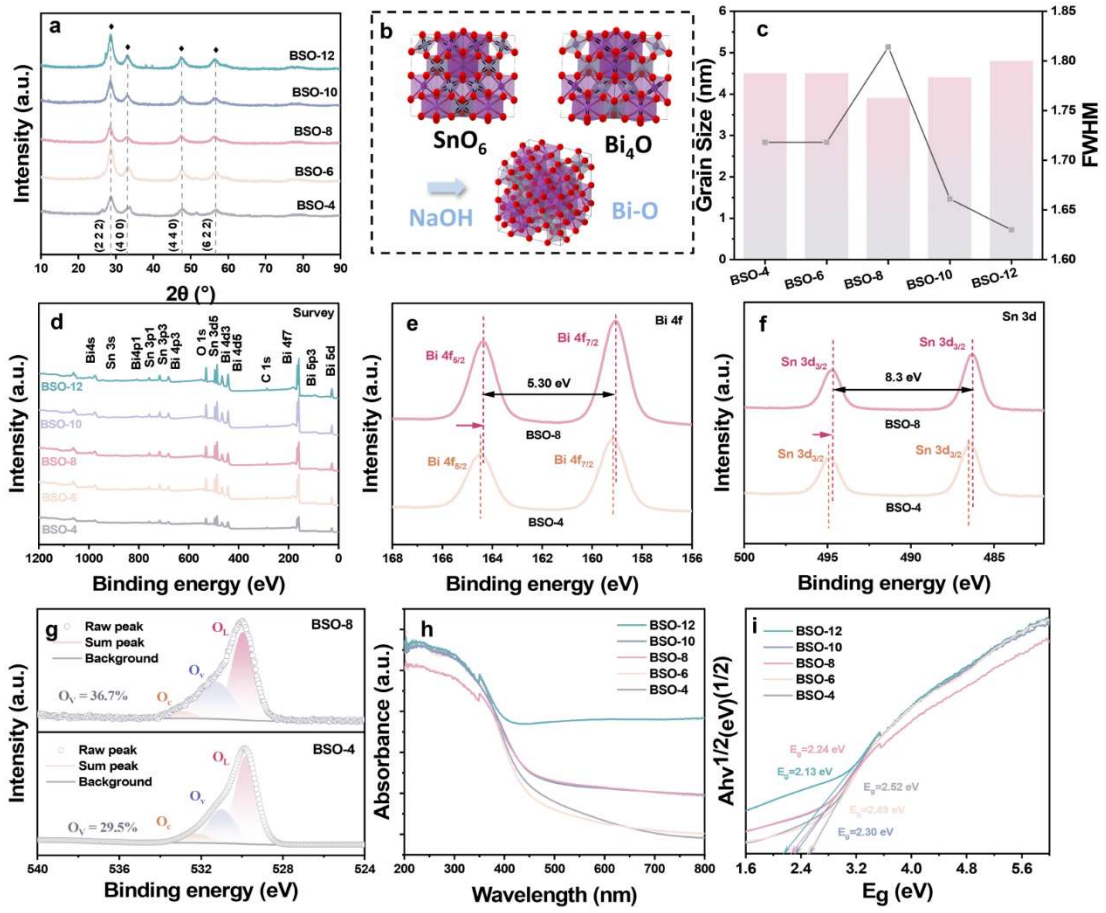

Figure 3. (a) XRD patterns of all samples, (b) Crystal structures of BSO, (c) Crystallite size distribution and (d) XPS survey spectra of all samples, High-resolution scan of (e) Bi 4f, (f) Sn 3d and (g) O1s of BSO-4 and BSO-8, (h) UV-vis absorption spectra and (i) Tauc plot of all samples.

The X-ray diffraction (XRD) patterns of all tested samples, recorded between 2θ angles of 20° and 80°, are displayed in Figure 3a. All observed diffraction peaks align with the PDF card for $Bi_2Sn_2O_7$, which is characterized as a cubic pyrochlore (JCPDS No.87-0284). These diffraction peaks correspond to bismuth stannate oxide (BSO) with the Fd-3m space group[20]. As illustrated in Figure 3b, cubic structure of BSO comprises octahedral SnO_6 units (exhibiting a shared-vertex configuration) and hexahedral Bi_2O_3 units (demonstrating a corner-sharing arrangement), both of which confer significant

advantages for electron transport. The presence of sodium hydroxide (NaOH) is critical for modulating the crystallization behavior of BSO. As shown in Figure S6, the BSO-X sample synthesized without NaOH lacks discernible characteristic diffraction peaks, indicating poor crystallinity. Furthermore, NaOH facilitates the etching of Bi-O bonds in BSO, thereby generating additional dangling bonds. An increase in NaOH concentration results in a slight peak shift to lower ~~higher~~ angles (according to the slow scan at 2°/min from 27° to 31°, as shown in Figure S7), which can be attributed to the etching effects of alkali that create more defects, consistent with the findings from photoelectron spectroscopy. Notably, all samples exhibit weak peak intensities coupled with narrowed full width at half maximum (FWHM) (Figure 3a), indicative of nanocrystallization within the grain structure. This observation aligns with previously reported TEM results. Crystallite size estimations, calculated using the Scherrer equation [21] (Equations S1), reveals that BSO-8 possesses the smallest grain dimensions among the series, suggesting optimal gas-sensitive performance (Figure 3c).

The surface chemical states and elemental composition were examined using XPS. The survey spectra (Figure 3d) exhibit characteristic peaks corresponding to photoelectrons emitted from energy levels, including C 1s (284.8 eV, calibrated for charge correction), Bi 5d, Bi 5p, Bi 4f, Bi 4d, Bi 4p, Bi 4s, Sn 3d, Sn 3p, Sn 3s, and O 1s levels. The XPS spectra recoded on the Bi 4f region (Figure 3e), reveal the characteristic doublet peaks of Bi^{3+}, whith components located at 164.3 eV (Bi $4f_{5/2}$) and 159.0 eV (Bi $4f_{7/2}$), exhibiting a spin-orbit coupling energy of 5.30 eV for BSO-8 (Figure 3e). In contrast, the Sn

3d spectra (Figure 3f) display the doublet with Sn 3d5/2 and Sn 3d3/2 componentes centered respectively at 494.7 eV and 486.4 eV, with a spin-orbit coupling energy of 8.3 eV, confirming the predominance of Sn^{4+} oxidation states [22,23]. A comparative analysis of BSO-4 and BSO-8 indicates slight shifts toward lower binding energies in both Bi 4f and Sn 3d peaks. This reduction in binding energy is likely attributable to an increased concentration of oxygen vacancies. The deconvolution of the O 1s spectra reveals three distinct components: one associated with chemisorbed oxygen (O_C), another with oxygen vacancies (OV), and a third with lattice oxygen (OL), centered at 532.9 eV, 531.3 eV, and 529.8 eV, respectively[24]. The relative concentration of oxygen vacancies in BSO-8 is determined to be 36.7% compared to 29.5% in BSO-4. The elevated relative concentration of oxygen vacancies can function as electron donors, thereby augmenting the free electron concentration within the material. In n-type semiconductors, the increased carrier density facilitates gas adsorption, enhancing to capture of electrons and promoting the adsorption of gas molecules (O_2) on the surface. This interaction leads to the formation of reactive oxygen species (O_2^-, O^-), which subsequently react with target gases to amplify the sensing signal[25]. The metal atoms exposed by oxygen vacancies potentially function as active centers, improving gas adsorption capability. These defect sites may also catalyze surface reactions by lowering the activation energy barrier.

The UV-Vis absorption spectra (Figure 3h) were used to elucidate the band

structure of the material. The bandgap (E_g) was determined using the Tauc plot method, represented by the equation $(\alpha hv)^{1/n}= B(hv-E_g)$ [26], where n is set to be 2, as $Bi_2Sn_2O_7$ is classified as an indirect bandgap semiconductor. The calculated bandgap values for BSO-4, BSO-6, BSO-8, and BSO-10, BSO-12were 2.52 eV, 2.49 eV, 2.30 eV, 2.24 eV, and 2.13 eV, respectively (Figure 3i). It was observed that the presence of defects leads to a progressive narrowing of the bandgap, thereby facilitating electron transitions between valence and condution band.

The specific surface area and pore size have a significant influence on gas-sensing performance. Nitrogen adsorption and desorption experiments were conducted to assess these parameters. From Brunauer-Emmett-Teller (BET) measurements (Figures. 4a-4c), the surface areas followed the sequence: BSO-4 (75.338 $m^2 g^{-1}$) < BSO-6 (89.430 $m^2 g^{-1}$) < BSO-12 (94.980 $m^2 g^{-1}$) < BSO-10 (129.493 $m^2 g^{-1}$) < BSO-8 (143.568 $m^2 g^{-1}$), respectively. The average pore diameters of BSO-4, BSO-6, BSO-8, BSO-10 and BSO-12 were determined to be 3.126, 3.129, 3.506, 3.314, and 3.136 nm, respectively. Additional BET results for other samples are present in Figure S8. Notably, BSO-8 exhibited the largest specific surface area of 143.568 m^2g^{-1}, and an average pore diameter of 3.51 nm. A larger specific surface area enhances the exposure of active sites on the surface of the material, thereby improving gas sensing performance. Conversely, variations in pore size appear to have a lesser impact compared to changes in specific surface area. For room-

temperature gas sensors, the specific surface area exerts a more substantial influence on sensing performance than pore size, as discussed in Section 4.

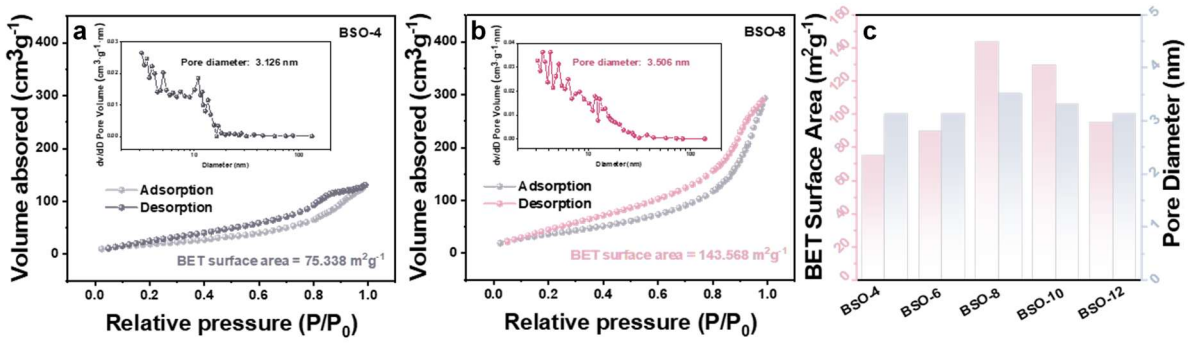

Figure 4. N_2 adsorption and desorption isotherms (the insert shows the distribution of pore size) of (a) BSO-4, (b) BSO-8, and (c) all samples.

Gas sensing properties. A gas sensing test was conducted using a homemade system. All tests were performed under RT (25 ± 2℃), 30%RH. Figures. 5a and 5b show sensor response curves to 1-octanol at concentrations ranging from 5 to 50 ppm. The experiment was conducted using three independent sensors (n=3), with each sensor fabricated from an independently synthesized material batch. It can be readily observed that the response values of the gas are positively correlated with the gas concentration, with BSO-8 demonstrating superior performance (average response values were 2.70±0.09, 4.25±0.23, 6.68±0.18, 11.26±0.26, 17.90±0.39, 32.60±0.59, 44.40±0.62, 75.06±1.25 at 5, 10, 15, 20, 25, 30, 40 and 50 ppm, respectively). To compare the performance of different BSO sensors, we performed a one-way analysis of variance (ANOVA) to statistically compare all five BSO sensors at each concentration point (5–50 ppm). The results revealed extremely significant

differences between groups (all P values < 0.0001). Subsequent Tukey's HSD post-hoc tests specifically compared the optimal BSO-8 sensor with other sensors. （as shown in Figure S2 and Table S2）, More responses values can be found in Table S1. The response values of different samples at varying concentrations of the target gas can be found in the supplementary materials. Within the range of 5 to 50 ppm, the gas concentration and response value show a nonlinear growth. The non-linear fitting line of all samples is shown in Figure 5c, where BSO-8 satisfies $y = 0.026x^2 + 2.03x + 1.31$, $R^2=0.99$, while the fitting data of all samples can be found in Table S3. Figure 5d delineates the response and recovery times at different concentrations. The response time fluctuates wildly at low concentrations, possibly due to insufficient occupation of active sites, resulting in an unstable response. At high concentrations, the active sites tend to be saturated, and the reaction rate slows down. The τ_{rec} continuously shortens as the concentration increases, which may be related to the accelerated desorption rate at high concentrations. The τ_{res} is always longer than the τ_{rec}, as the response process involves multiple steps of kinetics, such as gas diffusion, adsorption, and surface reactions. In contrast, the recovery process is mainly dominated by desorption and has a lower energy barrier.

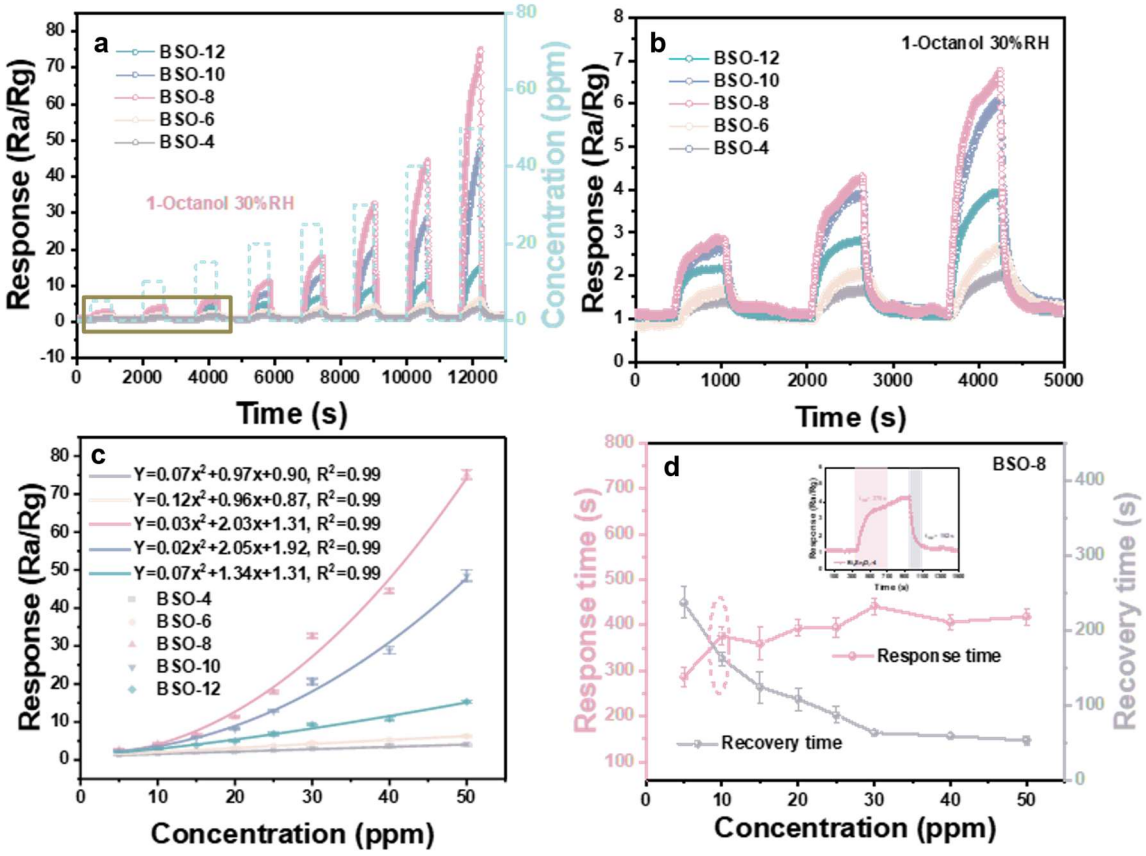

Figure 5. Response curves to (a) 5-50 ppm and (b) 5-15 ppm 1-octanol at 30%RH, (c) Fitting curves of all samples, and (d) Response/Recove0ry times of BSO-8 to 5-50 ppm 1-octanol at 30%RH. Error bars represent the standard deviation (SD), n = 3 independent measurements.

In practical applications, especially when used as a crop matter volatile gas, the released concentrations during their initial emission stages are typically extremely low (<10 ppm)[27–31]. Notably, the BSO-8 sensor maintains a detectable response within the 1–5 ppm range. The specific response values are depicted in Table S4. As illustrated in Figure 6a, the dynamic response of the sensor to 1-octanol across the 1–5 ppm concentration reveals a measurable response value of 1.07 at the lower detection threshold (1 ppm). The limit of

detection (LOD) was calculated using the slope (M) of the fitting curves (Figure 6b) and the sensor noise (σ), which was determined based on the baseline resistance of 50 consecutive measurements (N=50) from the corresponding sample (Equations S2 and S3)[32]. The results indicate that the LOD of the BSO-8 sensors is 100 ppb. Linear regression analysis of the sensor responses to 1-octanol over the 1–5 ppm concentration range (Figure 6b) reveals a significant linear correlation between gas concentration and response. The slope of the calibration curve quantifies the sensor sensitivity, with BSO-8 demonstrating superior performance through its linear regression model ($y=0.389x+0.677$, $R^2=0.99$). This result demonstrates the sensor's suitability for detecting low concentrations.

Humidity is a critical environmental factor that practical detection can't overlook. The BSO-8 gas sensor was tested against 5 ppm 1-octanol at varying humidity levels (30-90% RH). The results (Figures. 6c and d) demonstrate that the sensor's response progressively declines with increasing humidity, with the coefficient of variation (CV) of 59.1%, which was defined as $R_{SD}/R_{average}\times100\%$ (where R_{SD} and $R_{average}$ are the standard deviation and average value of responses with different humidity, respectively. $R_{SD}=2.2982$, $R_{average}=3.88667$). This finding is attributed to competitive adsorption between the target gas and water molecules on the sensor surface. Specifically, the preferential adsorption of water molecules reduces the availability of active chemisorption sites for the target gas, thereby diminishing the response signal.

Repeatability and long-term stability are critical performance metrics for gas sensors. Figure 6e displays the repeatability test of the BSO-8 sensor over 9 cycles at 10 ppm 1-octanol and 30% RH, with a SD of 0.55 (Equation S3). Figure 6f illustrates the long-term stability of the BSO-4 sensor exposed to 25 ppm 1-octanol over 1, 3, 5, 7, 9, and 14 days. This sensor demonstrated stability within two weeks, with a SD of 0.55, and the response value remained unchanged after 14 days.

Figure 6g illustrates the responses of the BSO-8 sensor to potential interfering gases in crop growth and storage environments at 30%RH, we selected the following interfering gases: (Z)-3-hexen-1-ol (a stress marker indicating pathogen or pest infestation during crop growth[33,34]), 1-octen-3-ol and ethyl acetate (characteristic volatile markers released during fungal contamination in storage[3]), and n-hexane (a residual chemical from post-harvest processing[35]). For concentration selection, (Z)-3-hexen-1-ol, n-hexane, and ethyl acetate were tested at 100 ppm to ensure a significant sensor response, as lower concentrations did not produce detectable signal variations. Additionally, 1-octen-3-ol was also examined at 30 ppm[36], reflecting its typical release level during early-stage mold activity, to better simulate real-world contamination scenarios. The responses are 16.3±0.9, 1.5±0.15, 1.2±0.1, and 1.8±0.12, respectively, three measurements were repeated with similar results. The BSO-8 sensor demonstrates good selectivity for 1-octanol.

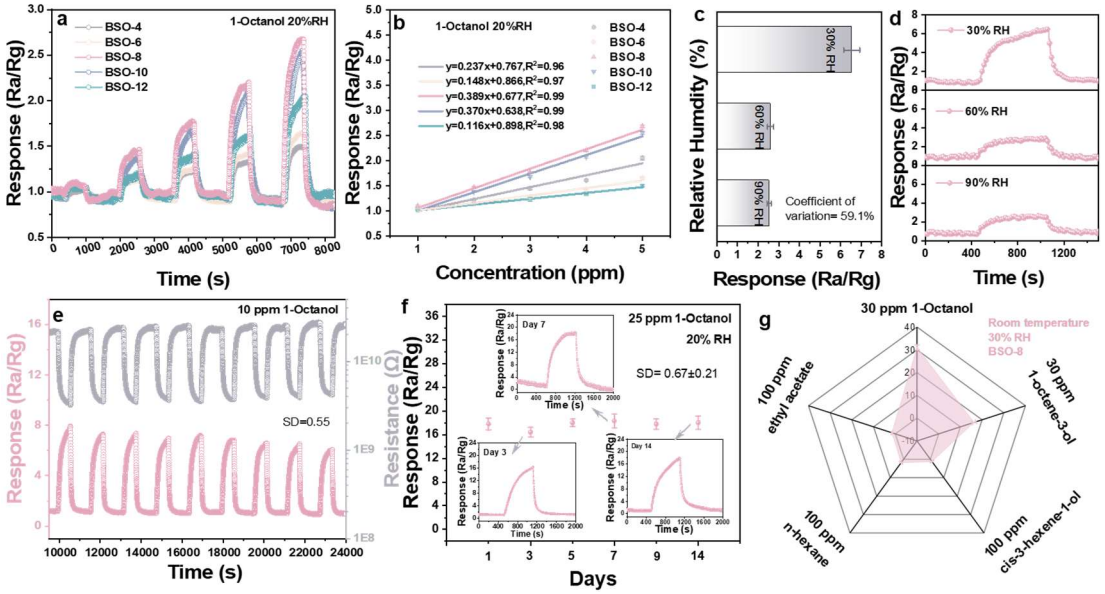

Figure 6. (a) Response curves and (b) Fitting curves to1-5 ppm 1-octanol at 30%RH, (c) Response value and (d) Real-time response curves at different RH (30% RH-90% RH), (e) Electrical resistance change and response change of the BSO-8 sensor in a continuous cycling test with 9 cycles, (f) Stability test of BSO-8 sensor with 25 ppm 1-octanol in 14 days, (g) Selectivity of the BSO-8 sensor with 30% RH. Error bars shown in (b), (c), and (e) indicate the SD based on n = 3 independent measurements.

Sensing Mechanism. The sensing mechanism of the BSO-based sensor for 1-octanol detection is illustrated in Figure 7a, based on oxygen adsorption theory, which operates via a chemiresistive behavior driven by gas-surface interactions and electron transfer dynamics. Upon exposure to ambient air, oxygen molecules with high electronegativity chemisorb onto the BSO surface (Equation 5), extracting electron-accepting surface states that reduce the conduction band electron density in this n-type material (where electrons are

the majority carriers). This process generates temperature-dependent adsorbed oxygen species (O_2^-, O^-, or O^{2-}), with O_2^- being the dominant ionic state at room temperature (Equation 6). The resultant electron depletion in the conduction band increases the electrical resistance of the baseline, leading to the expansion of electron depletion layers, which is dependent on the adsorbed gas concentration. Specifically, the electron transfer on the material surface is intrinsically governed by the individual grains of the material. When electrons migrate between grains, Schottky barriers form at grain boundaries, hindering electron transport. In the absence of gas exposure, the height of the Schottky barrier is determined by the material's work function. Upon oxygen adsorption, a negative charge accumulates on the material surface, causing upward band bending and an increase in Schottky barrier height. When exposed to reducing gases such as 1-octanol, surface redox reactions occur between gas molecules and chemisorbed oxygen ions (O_2^-). The reactions release trapped charge carriers into the semiconductor's conduction band, thereby enhancing the charge carrier density while simultaneously reducing the depletion layer width and lowering the potential barrier height. This effect ultimately reduces the sensor's electrical resistance, as described in Equation 7. From an electronic perspective, the sensing material can be regarded as a component with continuous impedance. The reduction in particle size plays a crucial role in enhancing the sensor response. Below the critical threshold of $2\lambda D$ (where λD represents the Debye length), the response of the gas sensor is significantly

enhanced [37].

$$O_{2(abs)} \leftrightarrow O_{2(abs)} \tag{5}$$

$$O_{2(abs)} + e^- \leftrightarrow O_2^-(ads)\left(T \le 150^\circ C\right) \tag{6}$$

$$CH_3(CH_2)_7OH + 12O_2^- \rightarrow 8CO_2 + 9H_2O + 12e^- \tag{7}$$

Moreover, the gas-sensing mechanism fundamentally involves interactions between gas molecules and the sensing layer, including gas diffusion, subsequent adsorption/desorption, and selective catalytic reduction (SCR) of gas molecules with the sensitive material within the nanostructured materials. According to Knudsen's diffusion [38] and Arrhenius Equation [39] (Equations 8 and 9), where D_k represents the diffusion coefficient, and the rate constant (k) denotes the SCR reaction rate, the SCR rate exhibits stronger temperature dependence compared to the gas diffusion rate [40]. At room temperature, catalytic reactions are more difficult to occur relative to gas diffusion [41]. Therefore, a high specific surface area (which can offer abundant active sites for reactions) plays a more important role in improving the performance of room-temperature sensors (by accelerating gas diffusion) than pore size, which is consistent with the previous characterization results.

$$Dk = \frac{4r}{3} \times \sqrt{\frac{2RT}{\pi M}} \tag{8}$$

$$k = A \times \exp\left(-\frac{E_a}{RT}\right) \tag{9}$$

Here, R, T, M, and E_a represent the gas constant, temperature, molar mass of gas molecules, and activation energy of the chemical reaction, respectively,

while *r* denotes the radius of gas molecules. The energy band diagram (Figure 7b) was calculated according to the valence band recorded using XPS to further investigate the electronic structure of BSO. The $E_{VB,NHE}$=1.80 eV and △V=2.54 eV can be calculated based on the difference between the x-coordinates of the tangent intersection and the inflection point, respectively, as shown in Figure 8c. According to Equations 10 and 11[42], the valence band maximum (E_{VB}) position of the sensor with optimal performance was determined to be 1.88 eV, with a work function (Φ) = 7.06 eV. Combined with the experimental bandgap width, the detailed energy band diagram was constructed.

$$E_{VB,NHE} = \varphi + E_{VB,XPS} - 4.44\ eV \quad (10)$$

$$\Delta V = \phi - \varphi \quad (11)$$

where the φ was the work function of the tester (4.52 eV), ΔV were the contact potential energy.

Furthermore, first-principles calculations were employed to elucidate the gas-sensing mechanism of BSO. Figures 6d and 6e present the total density of states (DOS) and projected density of states (PDOS) of Bi, Sn, and O atoms. BSO's valence band maximum (VBM) is predominantly composed of Bi 6p and O 2p orbitals, while the conduction band minimum (CBM) primarily originates from O 2p orbitals. During electron transfer processes, electrons transition from the O 2p orbitals to hybridized orbitals formed by Bi 6p and O 2p states, participating in chemical reactions with target gas.

Additionally, adsorption models of 1-octanol molecules on the BSO (222)

surface were computed. Distinct adsorption configurations (M1-M8, Figure S10) were investigated, including different adsorption sites and orientations. The adsorption energies (E_{ads}) and electron transfer were calculated for all models, as summarized in Figure 7f. All adsorption configurations exhibit spontaneous behavior, as confirmed by the negative adsorption energy values. This indicates that the adsorption process is energetically favorable and exothermic[43]. Additionally, it can be observed that the adsorption sites have no significant effect on 1-octanol adsorption on the BSO surface, as evidenced by the negligible differences in adsorption energy and electron transfer, this suggests that the adsorption configuration has little effect on the interaction between the material and the gas molecules[44]. Among them, the M4 model exhibits the lowest adsorption energy and the highest electron transfer, representing the most stable adsorption configuration. This suggests that the adsorption configuration has little effect on the interaction between the material and the gas[45]. The distance between the gas molecule and the material surface is 2.605 Å (Bi-O bond), as described in Figure 7g. Before and after gas adsorption, certain changes occur in the bond lengths of the gas molecule as shown in Figure S9, the C-C and C-O bonds of the 1-octanol molecule ~~elongte~~ elongate, while the C-H and O-H bonds shorten after adsorption. During the adsorption of 1-octanol on the $Bi_2Sn_2O_7$ surface, intramolecular charge redistribution occurs, primarily due to electron transfer from the hydroxyl (–OH) oxygen atom to the surface via Lewis acid–base interaction, leading to strong adsorption.

This weakens and elongates the C–O and adjacent C–C bonds as electrons are drawn toward the surface. Conversely, increased electron density around the O–H bond and polarization effects strengthen the C–H and O–H bonds, resulting in their contraction[46,47]. The differential charge density (EDD) map of the M4 model was further employed to examine electron transfer in the adsorption system (Figure 7h). In the electron density difference (EDD) map, red regions signify electron depletion (loss of electrons). In contrast, blue regions denote electron accumulation (gain of electrons). The results reveal that electron transfer during the adsorption process on the BSO surface is primarily concentrated between the region above the Bi atom and the area below the O atom of 1-octanol, indicating a localized charge redistribution mediated by the interaction between the molecule and the surface.

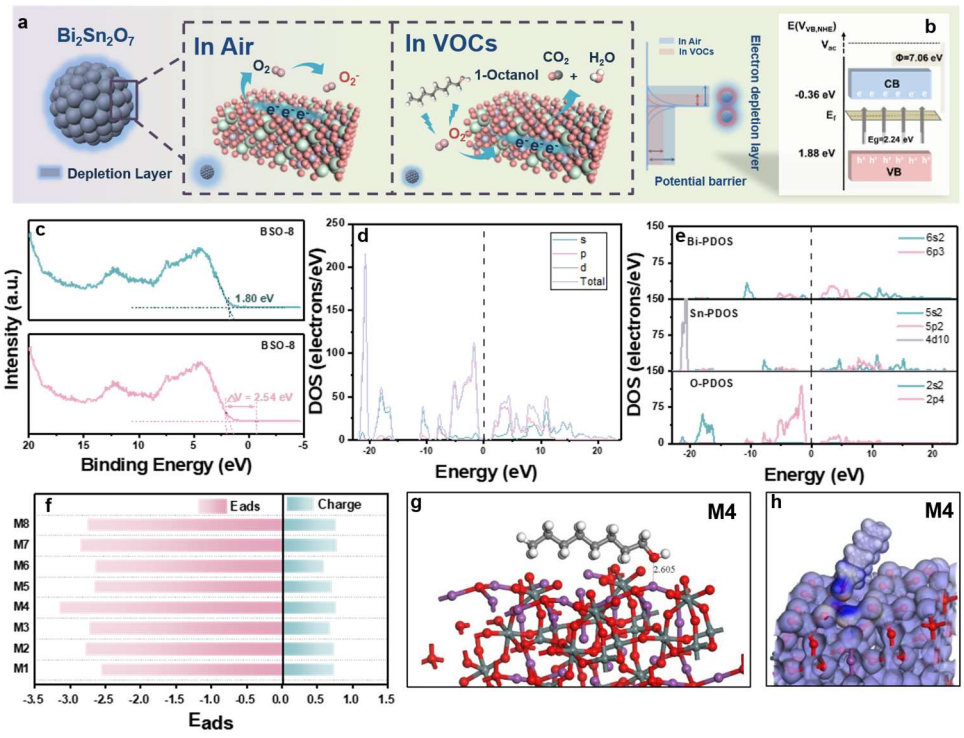

Figure 7. (a) The gas sensing mechanism for the BSO sensor, (b) The band

structure and (c) The VBXPS spectrum of BSO-8, (d) DOS and (e) PDOS of BSO models, (f) Adsorption energy and electron transfer of M1-M8, (g) After adsorption configuration and (h) EDD spectra of M4.

Conclusion

This study presents the development of a room-temperature gas sensor utilizing bismuth stannate oxide (BSO) quantum dots (QDs) characterized by a high density of oxygen vacancies and an extensive specific surface area. The BSO QDs were synthesized through a hydrothermal method for the detection of 1-octanol across a broad concentration range of 1 to 50 parts per million (ppm). The BSO-8 sensor demonstrated a remarkable response to 1-octanol, achieving a response value of 75.06 at 80 ppm under 30% relative humidity, with a limit of detection (LOD) of 100 parts per billion (ppb). Furthermore, the sensor exhibited outstanding repeatability, with a SD of 0.67 over nine measurement cycles, and long-term stability characterized by a SD of 0.55 over a period of 14 days, alongside favorable selectivity towards the target gas. Characterization results indicate that the enhanced room-temperature sensing performance of the BSO-8 sensor is likely attributable to its unique crystal structure, sub-nanoscale dimensions (approximately 4 to 5 nm), high defect density (oxygen vacancies at 36.7%), and ultra-large specific surface area (BET= 143.57 m^2g^{-1}). Additionally, density functional theory (DFT) calculations, in conjunction with band structure analysis, suggest that the superior room-temperature detection capability of BSO for 1-octanol is primarily due to surface

reactions that are facilitated by the extensive specific surface area, which outweighs the influence of pore size diffusion, as well as the electron transfer processes occurring between the gas molecules and the material's surface.

Supporting Information

Supporting Information Available: The following file is available free of charge.

Supporting Information (DOCX). The Supporting Information includes: calculation details for the Scherrer equation, statistical parameters (SD) and sensor performance metrics (LOD); four supplementary tables (Tables S1–S4) listing response values, statistical comparisons, and fitting parameters across 1–5 ppm and 5-80 ppm 1-octanol; and ten supplementary figures (Figures S1–S10) showing structural models, TEM/SEM/XRD/EDX characterization, adsorption/desorption isotherms, adsorption configurations, and statistical performance comparisons of the BSO sensors.

Author Information

Corresponding Author

Chao Zhang – *College of Mechanical Engineering, Yangzhou University, Yangzhou 225127, China; orcid.org/00000003-2346-6770; Phone: +86-514-87436008; Email: zhangc@yzu.edu.cn*

Authors

Yiwen Zhou – *College of Mechanical Engineering, Yangzhou University, Yangzhou 225127, China; Jiangsu Key Laboratory of Surface Strengthening*

and Functional Manufacturing, Yangzhou University, Yangzhou 225127, PR China; orcid.org/0009-0001-6956-3376

Zichen Zheng – *College of Mechanical Engineering, Yangzhou University, Yangzhou 225127, China; Jiangsu Key Laboratory of Surface Strengthening and Functional Manufacturing, Yangzhou University, Yangzhou 225127, PR China; Service de Science des Matériaux, Faculté Polytechnique, Université de Mons, Mons 7000, Belgium*

Kewei Liu – *College of Mechanical Engineering, Yangzhou University, Yangzhou 225127, China; Jiangsu Key Laboratory of Surface Strengthening and Functional Manufacturing, Yangzhou University, Yangzhou 225127, PR China;*

Marc Debliquy − *Service de Science des Matériaux, Faculté Polytechnique, Université de Mons, Mons 7000, Belgium*

Carla Bittencourt − *Chimie des Interactions Plasma-Surface, Research Institute for Materials Science and Engineering, University of Mons, 7000 Mons, Belgium*

Author Contributions

Yiwen Zhou: Conception, Methodology, Investigation, Writing – original draft. **Zichen Zheng:** Investigation, Writing – review & editing. **Kewei Liu:** Writing – review & editing. **Marc Debliquy:** Writing – review & editing. **Carla Bittencourt:** Writing – review & editing. **Chao Zhang:** Conceptualization, Methodology, Supervision, Writing – review & editing, Funding acquisition.

Notes

The authors declare no competing financial interest.

Acknowledgments

This work was supported by the Outstanding Youth Foundation of Jiangsu Province of China (Grant No. BK20211548), the Yangzhou Science and Technology Plan Project (Grant No. YZ2023246) and the Postgraduate Research & Practice Innovation Program of Jiangsu Province (Grant No. KYCX25_395).

References

(1) Duan, W.-Y.; Qin, Y.-L.; Zhang, S.-B.; Zhai, H.-C.; Lv, Y.-Y.; Wei, S.; Ma, P.-A.; Hu, Y.-S. Inhibitory Mechanisms of Plant Volatile 1-Octanol on the Germination of Aspergillus Flavus Spores. *Food Biophys.* **2024**, *19* (1), 96–108.

(2) Li, H.; Guo, T.; Luo, Z.; Chen, J.; Xie, X.; Ahammed, G. J.; Liu, A.; Chen, S. Volatile Organic Compounds from Irpex Lacteus Inhibit Pathogenic Fungi and Enhance Plant Resistance to Botrytis Cinerea in Tomato. *Microbiol. Res.* **2025**, *297*, 128188.

(3) Liu, K.; Zhang, C.; Xu, J.; Liu, Q. Research Advance in Gas Detection of Volatile Organic Compounds Released in Rice Quality Deterioration Process. *Compr. Rev. Food Sci. F.* **2021**, *20* (6), 5802–5828.

(4) Zheng, Z.; Liu, K.; Zhou, Y.; Xu, K.; Wang, C.; Debliquy, M.; Bittencourt, C.; Zhang, C. CuO-Decorated Bismuth Subcarbonate p-n Heterostructured Micro-Flowers for High-Selectivity VOC Gas Sensor Arrays and Cooked Rice Quality

Assessment. *J. Adv. Ceram.* **2025**.

(5) Qu, L.; Zhao, Y.; Li, Y.; Lv, H. Effect of Storage Temperature on the Quality of Brown Rice Revealed by Integrated GC–MS and Lipidomics Analysis. *Food Chem.* **2025**, *465*, 142107.

(6) Wu, K.; Debliquy, M.; Zhang, C. Room Temperature Gas Sensors Based on Ce Doped TiO2 Nanocrystals for Highly Sensitive NH_3 Detection. *Chem. Eng. J.* **2022**, *444*, 136449.

(7) Sui, N.; Wei, X.; Cao, S.; Zhang, P.; Zhou, T.; Zhang, T. Nanoscale Bimetallic AuPt-Functionalized Metal Oxide Chemiresistors: Ppb-Level and Selective Detection for Ozone and Acetone. *ACS Sens.* **2022**, *7* (8), 2178–2187.

(8) Xu, K.; Han, M.; Zheng, Z.; Yu, Z.; Liao, H.; Sun, H.; Zhang, C. Well-Designed g-C_3N_4 Nanosheet Incorporated Ag Loaded $Er_{0.05}La_{0.95}FeO_3$ Heterojunctions for Isoamyl Alcohol Detection. *J. Adv. Ceram.* **2024**, *13* (6), 736–745.

(9) He, X.; Xu, J.; Bian, Y.; Tulliani, J.-M.; Zhang, C. Lychee-like Bi_2MoO_6 Spheres for Highly Sensitive Room-Temperature Phosphine Sensing. *ACS Sens.* **2025**, *10* (4), 2617–2626.

(10) Deb, S.; Mondal, A.; Ashok Kumar Reddy, Y. Review on Development of Metal-Oxide and 2-D Material Based Gas Sensors under Light-Activation. *Curr. Opin. Solid State Mater. Sci.* **2024**, *30*, 101160.

(11) Wu, K.; Xu, Z.; Xu, K.; Xu, J.; Luo, Y.; Debliquy, M.; Zhang, C. Oxygen Vacancy-Rich Engineering-Optimized Molybdenum Trioxide Microbelts for Room-Temperature Ppb-Level Trimethylamine Detection. *J. Adv. Ceram.* **2025**, *14* (7),

9221102.

(12) Yan, W.; Zhang, Y.; Bi, Y. Subnanometric Bismuth Clusters Confined in Pyrochlore-$Bi_2Sn_2O_7$ Enable Remarkable CO2 Photoreduction. *Angew. Chem. - Int. Ed.* **2024**, *63* (3), e202316459.

(13) Gao, S.; Wu, R.; Sun, M.; Guo, M.; DuBois, D. B.; Chen, S.; Ji, H.; Wang, C.; Wang, Q. High-Performance Nitrogen Photofixation by $Bi_2Sn_2O_7$ Nanoparticles Enriched with Oxygen Vacancies. *Appl. Catal., B* **2023**, *324*, 122260.

(14) Zhang, Y.; Di, J.; Qian, X.; Ji, M.; Tian, Z.; Ye, L.; Zhao, J.; Yin, S.; Li, H.; Xia, J. Oxygen Vacancies in $Bi_2Sn_2O_7$ Quantum Dots to Trigger Efficient Photocatalytic Nitrogen Reduction. *Appl. Catal., B* **2021**, *299*, 120680.

(15) Rahim, W.; Skelton, J. M.; Scanlon, D. O. α-$Bi_2Sn_2O_7$: A Potential Room Temperature n-Type Oxide Thermoelectric. *J. Mater. Chem.A* **2020**, *8* (32), 16405–16420.

(16) Zheng, Z.; Liu, K.; Zhou, Y.; Xu, K.; Luo, Y.; Ding, J.; Bittencourt, C.; Debliquy, M.; Zhang, C. Decorated-Induced Oxygen Vacancy Engineering for Ultra-Low Concentration Nonanal Sensing: A Case Study of La-Decorated $Bi_2O_2CO_3$. *Adv. Sci.* **2024**, *11* (43), 2408096.

(17) Zheng, Z.; Liu, K.; Zhou, Y.; Xu, K.; Debliquy, M.; Zhang, C. Room-Temperature Sensing Mechanism of Gqds/$Bisbo_4$ Nanorod Clusters: Experimental and Density Functional Theory Study. *ACS Sens.* **2024**, *9* (6), 3346–3356.

(18) Wang, Z.; Hu, X.; Zhou, Y. Accelerated Screening of Highly Sensitive Gas Sensor Materials for Greenhouse Gases Based on DFT and Machine Learning Methods.

ACS Sens. **2025**, *10* (1), 563–572.

(19) Dong, W.; Sun, Y.; Hua, W.; Yao, Y.; Zhuang, G.; Lv, X.; Ma, Q.; Zhao, D. Preparation of Secondary Mesopores in Mesoporous Anatase–Silica Nanocomposites with Unprecedented-High Photocatalytic Degradation Performances. *Adv. Funct. Mater.* **2016**, *26* (6), 964–976.

(20) Lu, Y.; Chen, M.; Huang, T.; Huang, Y.; Cao, J.; Li, H.; Ho, W.; Lee, S. C. Oxygen Vacancy-Dependent Photocatalytic Activity of Well-Defined $Bi_2Sn_2O_{7-x}$ Hollow Nanocubes for NO_x Removal. *Environ. Sci.: Nano* **2021**, *8* (7), 1927–1933.

(21) Zhang, C.; Liu, K.; Zheng, Z.; Debliquy, M. Defect Engineering of Nanostructured ZnSnO3 for Conductometric Room Temperature CO2 Sensors. *Sensors and Actuators B: Chemical* **2023**, *384*, 133628.

(22) Huang, S.; Kou, X.; He, D.; Du, C.; Wang, X.; Su, Y. Oxygen-Vacancy-Mediated Photocatalysis over $Bi_2Sn_2O_7$: Exceptional Catalytic Activity and Selectivity. *ChemCatChem* **2019**, *11* (24), 6316–6323.

(23) Sruthi, L.; Okla, M. K.; Janani, B.; Abdel-Maksoud, M. A.; Saleh, I. A.; Abu-Harirah, H. A.; Khan, S. S. Construction of rGO-$Bi_2Sn_2O_7$-$NiFe_2O_4$ Nanoheterojunction System for the Enhanced Photodegradation of Doxycycline: A Brief Insight on Degradation Kinetics and Toxicological Evaluation on Allium Cepa. *J. Cleaner Prod.* **2024**, *434*, 139936.

(24) Zhu, S.; Fan, H.; Su, Y.; Fan, Y.; Wang, W. Ultrahigh Triethylamine Sensitivity of WO_3-MoO_3 n-n Heterojunction Sensor Operating at Low-Temperature. *Chem. Eng. J.* **2025**, *507*, 160607.

(25) Ji, H.; Zeng, W.; Li, Y. Gas Sensing Mechanisms of Metal Oxide Semiconductors: A Focus Review. *Nanoscale* **2019**, *11* (47), 22664–22684.

(26) Zheng, Z.; Liu, K.; Debliquy, M.; Zhang, C. Carbon Functionalized Cladding Bismuth Tungstate-Based 3D Twisted Micro-Flowers for Benzaldehyde Detection under Ultraviolet Light Excitation. *Sens. Actuators B Chem.* **2024**, *415*, 135982.

(27) Javidipour, I.; Qian, M. C. Volatile Component Change in Whey Protein Concentrate during Storage Investigated by Headspace Solid-Phase Microextraction Gas Chromatography. *Dairy Sci. Technol.* **2008**, *88* (1), 95–104.

(28) Thong, K.; Egi, N.; Tanaka, T.; Hirao, K.; Sopheap, E.; Thavrak, H.; Murakami, M.; Saio, K. Primary Volatile Aroma Compounds in Phka Rumduol, Cambodia. *JFNS* **2021**, *9* (1), 10.

(29) Taiti, C.; Vinciguerra, V.; Graziano, M. M.; Masi, E.; Garzoli, S. In-Depth Investigation of the Chemical Profile of Pelargonium Odoratissimum (L.) L'Hér. Hydrolate by SPME-GC/MS, GC/MS, LVI-GC/MS and PTR-Tof-MS Techniques. *Chemosensors* **2025**, *13* (9), 325.

(30) Lee, B.; Lin, P.; Cha, H. soo; Luo, J.; Chen, F. Characterization of Volatile Compounds in Cowart Muscadine Grape (Vitis Rotundifolia) during Ripening Stages Using GC-MS Combined with Principal Component Analysis. *Food Sci. Biotechnol.* **2016**, *25* (5), 1319–1326.

(31) Hamilton-Kemp, T. R.; Andersen, R. A.; Rodriguez, J. G.; Loughrin, J. H.; Patterson, C. G. Strawberry Foliage Headspace Vapor Components at Periods of Susceptibility and Resistance toTetranychus Urticae Koch. *J. Chem. Ecol.*

1988, *14* (3), 789–796.

(32) Zhou, Y.; Luo, Y.; Zheng, Z.; Liu, K.; He, X.; Wu, K.; Debliquy, M.; Zhang, C. Urchin-like Na-Doped Zinc Oxide Nanoneedles for Low-Concentration and Exclusive VOC Detections. *J. Adv. Ceram.* **2024**, *13* (4), 507–517.

(33) Ang, M. C.-Y.; Lew, T. T. S. Non-Destructive Technologies for Plant Health Diagnosis. *Front. Plant Sci.* **2022**, *13*.

(34) Li, Z.; Paul, R.; Ba Tis, T.; Saville, A. C.; Hansel, J. C.; Yu, T.; Ristaino, J. B.; Wei, Q. Non-Invasive Plant Disease Diagnostics Enabled by Smartphone-Based Fingerprinting of Leaf Volatiles. *Nat. Plants* **2019**, *5* (8), 856–866.

(35) Cravotto, C.; Claux, O.; Bartier, M.; Fabiano-Tixier, A.-S.; Tabasso, S. Leading Edge Technologies and Perspectives in Industrial Oilseed Extraction. *Molecules* **2023**, *28* (16), 5973..

(36) Zheng, Z.; Liu, K.; Zhou, Y.; Xu, K.; Luo, Y.; Ding, J.; Bittencourt, C.; Debliquy, M.; Zhang, C. Decorated-Induced Oxygen Vacancy Engineering for Ultra-Low Concentration Nonanal Sensing: A Case Study of La-Decorated $Bi_2O_2CO_3$. *Adv. Sci.* **2024**, *11* (43), 2408096.

(37) Kesler, V.; Murmann, B.; Soh, H. T. Going beyond the Debye Length: Overcoming Charge Screening Limitations in Next-Generation Bioelectronic Sensors. *ACS Nano* **2020**, *14* (12), 16194–16201.

(38) Gao, Y.; Zhu, H.; Wang, X.; Shen, R.; Zhou, X.; Zhao, X.; Li, Z.; Zhang, C.; Lei, F.; Yu, J. Promising Mass-Productive 4-Inch Commercial SERS Sensor with Particle in Micro-Nano Porous Ag/Si/Ag Structure Using in Auxiliary Diagnosis of

Early Lung Cancer. *Small* **2023**, *19* (25), 2207324.

(39) Malek, K.; Coppens, M.-O. Knudsen Self- and Fickian Diffusion in Rough Nanoporous Media. *J. Chem. Phys.* **2003**, *119* (5), 2801–2811.

(40) Sakai, G.; Matsunaga, N.; Shimanoe, K.; Yamazoe, N. Theory of Gas-Diffusion Controlled Sensitivity for Thin Film Semiconductor Gas Sensor. *Sens. Actuators B Chem.* **2001**, *80* (2), 125–131.

(41) Wang, X.; Wang, Y.; Tian, F.; Liang, H.; Wang, K.; Zhao, X.; Lu, Z.; Jiang, K.; Yang, L.; Lou, X. From the Surface Reaction Control to Gas-Diffusion Control: The Synthesis of Hierarchical Porous SnO_2 Microspheres and Their Gas-Sensing Mechanism. *J. Phys. Chem. C* **2015**, *119* (28), 15963–15976.

(42) Li, X.; Kang, B.; Dong, F.; Zhang, Z.; Luo, X.; Han, L.; Huang, J.; Feng, Z.; Chen, Z.; Xu, J.; Peng, B.; Wang, Z. L. Enhanced Photocatalytic Degradation and H_2/H_2O_2 Production Performance of S-pCN/WO2.72 S-Scheme Heterojunction with Appropriate Surface Oxygen Vacancies. *Nano Energy* **2021**, *81*, 105671.

(43) Zhang, D.; Wu, J.; Li, P.; Cao, Y.; Yang, Z. Hierarchical Nanoheterostructure of Tungsten Disulfide Nanoflowers Doped with Zinc Oxide Hollow Spheres: Benzene Gas Sensing Properties and First-Principles Study. *ACS Appl. Mater. Interfaces* **2019**, *11* (34), 31245–31256.

(44) Zhang, D.; Yang, Z.; Li, P.; Pang, M.; Xue, Q. Flexible Self-Powered High-Performance Ammonia Sensor Based on Au-Decorated $MoSe_2$ Nanoflowers Driven by Single Layer MoS_2-Flake Piezoelectric Nanogenerator. *Nano Energy* **2019**, *65*, 103974.

(45) Zhang, D.; Yu, S.; Wang, X.; Huang, J.; Pan, W.; Zhang, J.; Meteku, B. E.; Zeng, J. UV Illumination-Enhanced Ultrasensitive Ammonia Gas Sensor Based on (001)TiO2/MXene Heterostructure for Food Spoilage Detection. *J. Hazard. Mater.* **2022**, *423*, 127160.

(46) Zhang, D.; Yang, Z.; Yu, S.; Mi, Q.; Pan, Q. Diversiform Metal Oxide-Based Hybrid Nanostructures for Gas Sensing with Versatile Prospects. *Coord. Chem. Rev.* **2020**, *413*, 213272.

(47) Zhang, D.; Wu, J.; Li, P.; Cao, Y. Room-Temperature SO_2 Gas-Sensing Properties Based on a Metal-Doped MoS_2 Nanoflower: An Experimental and Density Functional Theory Investigation. *J. Mater. Chem.A* **2017**, *5* (39), 20666–20677.

The table of contents

A room-temperature 1-octanol sensor is proposed based on large surface area $Bi_2Sn_2O_7$ quantum dots. The sensor exhibited high sensitivity, stability and selectivity, the results revealed that $Bi_2Sn_2O_7$ sensor was available for large scale dynamic 1-octanol monitoring, highlighting its significance as a key biomarker for agricultural VOCs.

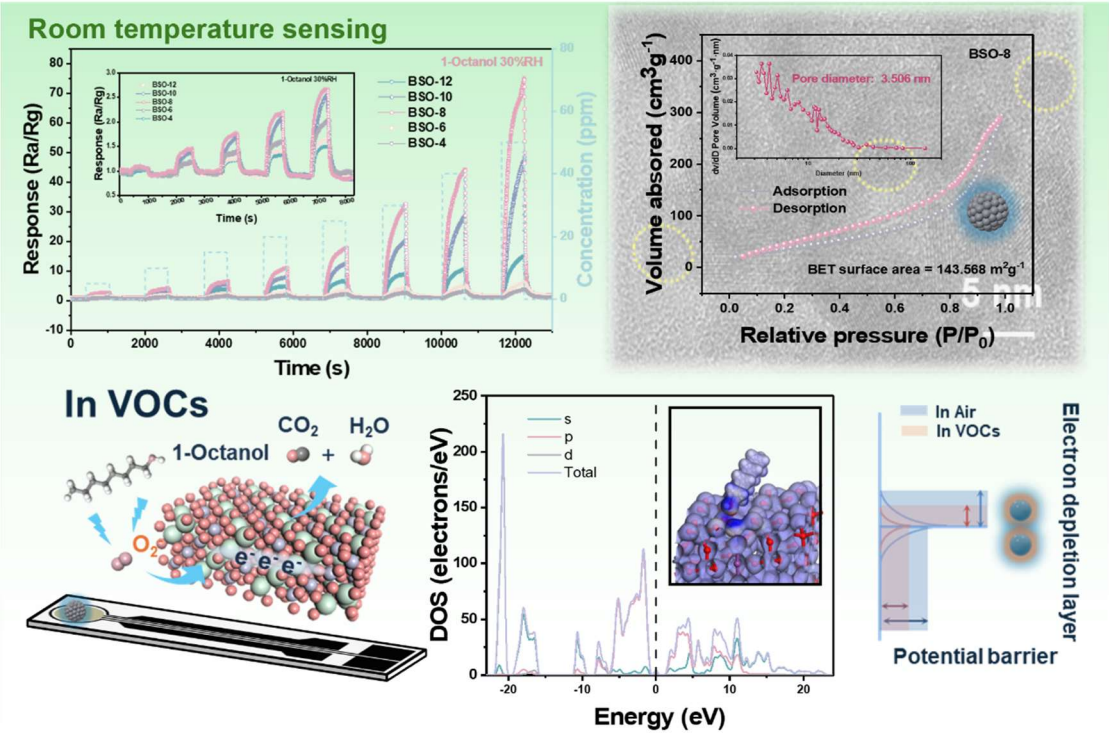

For TOC only